

Decadal and annual variations in meteoric flux from Ulysses, Wind, and SOFIE observations

Mark E. Hervig¹, David M. Malaspina², Veerle Jasmin Sterken³, Lynn B Wilson III⁴, Silvan Hunziker⁵, and Scott Martin Bailey⁶

¹GATS Inc.

²University of Colorado Boulder

³Eidgenoessische Technische Hochschule

⁴NASA Goddard Space Flight Center

⁵Swiss Federal Institute of Technology

⁶Virginia Polytechnic Institute and State University, Blacksburg, VA

November 26, 2022

Abstract

Our solar system is filled with meteoric particles, or cosmic dust, which is either interplanetary or interstellar in origin. Interstellar dust (ISD) enters the heliosphere due to the relative motion of the sun and the interstellar flow. Interplanetary dust (IPD) comes primarily from asteroid collisions or comet sublimation, and comprises the bulk of material entering Earth's atmosphere. This study examines variations in ISD and the IPD flux at Earth using observations from three different satellite techniques. First are size-resolved in situ meteoroid detections by the Ulysses spacecraft, and second are in situ indirect dust observations by Wind. Third are measurements of meteoric smoke in the mesosphere by the Solar Occultation For Ice Experiment (SOFIE). Wind observations are sorted into the interstellar and interplanetary components. Wind ISD show the anticipated correlation to the 22-yr. solar magnetic cycle, and are consistent with model predictions of ISD. Because Wind does not discriminate particle size, the IPD measurements were interpreted using meteoric mass distributions from Ulysses observations and from different models. Wind observations during 2007-2020 indicate a total meteoric influx at Earth of 22 metric tons per day ($t d^{-1}$), in reasonable agreement with long-term averages from SOFIE ($25 t d^{-1}$) and Ulysses ($32 t d^{-1}$). The SOFIE and Wind influx time series both show an unexpected correlation to the 22-yr. solar cycle. This relationship could be an artifact, or may indicate that IPD responds to changes in the solar magnetic field.

1 **Decadal and annual variations in meteoric flux from Ulysses, Wind, and**
2 **SOFIE observations**

3 Mark E. Hervig¹, David Malaspina^{2,3}, Veerle Sterken⁴, Lynn B. Wilson III⁵, Silvan Hunziker⁴,
4 and Scott M. Bailey⁶

5 ¹GATS, Driggs, Idaho, USA.

6 ²Laboratory for Atmospheric and Space Physics, University of Colorado, Boulder, Colorado, USA

7 ³Astrophysical and Planetary Sciences Department, University of Colorado, Boulder, Colorado,
8 USA

9 ⁴Institute for Particle Physics and Astrophysics, Swiss Federal Institute of Technology, Zürich,
10 Switzerland.

11 ⁵NASA Goddard Spaceflight Center, Greenbelt, Maryland, USA

12 ⁶Virginia Polytechnic Institute, Blacksburg, Virginia, USA.

13

14

15 **Main Points:**

16 1) SOFIE, Wind, and Ulysses give consistent estimates of the meteoric influx at Earth.

17 2) Annual and decadal variations in Wind interstellar dust observations agree with simulations.

18 3) Both interstellar and interplanetary dust are correlated to the 22-yr. solar magnetic cycle.

19

20 Keywords: Meteoric influx, SOFIE, Wind, Ulysses, interstellar dust, meteoric smoke

21 **Abstract.** Our solar system is filled with meteoric particles, or cosmic dust, which is either
22 interplanetary or interstellar in origin. Interstellar dust (ISD) enters the heliosphere due to the
23 relative motion of the sun and the interstellar flow. Interplanetary dust (IPD) comes primarily from
24 asteroid collisions or comet sublimation, and comprises the bulk of material entering Earth's
25 atmosphere. This study examines variations in ISD and the IPD flux at Earth using observations
26 from three different satellite techniques. First are size-resolved in situ meteoroid detections by the
27 Ulysses spacecraft, and second are in situ indirect dust observations by Wind. Third are
28 measurements of meteoric smoke in the mesosphere by the Solar Occultation For Ice Experiment
29 (SOFIE). Wind observations are sorted into the interstellar and interplanetary components. Wind
30 ISD show the anticipated correlation to the 22-yr. solar magnetic cycle, and are consistent with
31 model predictions of ISD. Because Wind does not discriminate particle size, the IPD
32 measurements were interpreted using meteoric mass distributions from Ulysses observations and
33 from different models. Wind observations during 2007-2020 indicate a total meteoric influx at
34 Earth of 22 metric tons per day ($t d^{-1}$), in reasonable agreement with long-term averages from
35 SOFIE ($25 t d^{-1}$) and Ulysses ($32 t d^{-1}$). The SOFIE and Wind influx time series both show an
36 unexpected correlation to the 22-yr. solar cycle. This relationship could be an artifact, or may
37 indicate that IPD responds to changes in the solar magnetic field.

38 **1. Introduction**

39 The solar system is filled with meteoric particles, or cosmic dust, which is interplanetary
40 or interstellar in origin. Interplanetary dust (IPD) comes from asteroid collisions or comet
41 sublimation, and is typically bound to solar orbits on the ecliptic plane. Interstellar dust (ISD)
42 enters the heliosphere due to the relative motion of the sun within the local interstellar cloud
43 [Krueger *et al.*, 2019; Sterken *et al.*, 2019]. Meteoroids are constantly entering Earth’s atmosphere,
44 with larger IPD particles dominating the mass influx. Frictional heating during entry vaporizes a
45 fraction of the particles at altitudes from ~80 to 100 km, and ablation products combine to form
46 nanometer sized meteoric smoke particles that reside in the mesosphere and stratosphere [Plane *et*
47 *al.*, 2012; Hervig *et al.*, 2017]. Smoke in the mesosphere is enhanced during polar winter due to
48 transport by the mesospheric meridional circulation, as indicated by models [Megner *et al.*, 2008]
49 and satellite observations [Hervig *et al.*, 2009]. Recent estimates of the meteoric influx into Earth’s
50 atmosphere range from ~15 - 60 metric tons per day (t d^{-1}) [e.g., Carrillo-Sánchez *et al.*, 2020], an
51 improvement over the bewildering range of previous decades (1 - 300 t d^{-1}) [e.g., Plane *et al.*,
52 2012]. The meteoric influx at Earth has implications for atmospheric chemistry, aerosol processes,
53 and ocean productivity [e.g., Rudraswami *et al.*, 2021], motivating further improvements to the
54 understanding of IPD influx and its variability.

55 The present study examines meteoric flux in the near-Earth environment using
56 observations from Ulysses, Wind, and the Solar Occultation For Ice Experiment (SOFIE). The
57 Wind and Ulysses spacecraft offer long-term records of in situ dust measurements, which are
58 related here to meteoric smoke measurements from the SOFIE satellite instrument. Interpreting
59 the Ulysses, Wind, and SOFIE measurements requires an understanding of the meteoric mass
60 distribution, and dust enhancement due to Earth’s gravity and size. The Ulysses and Wind

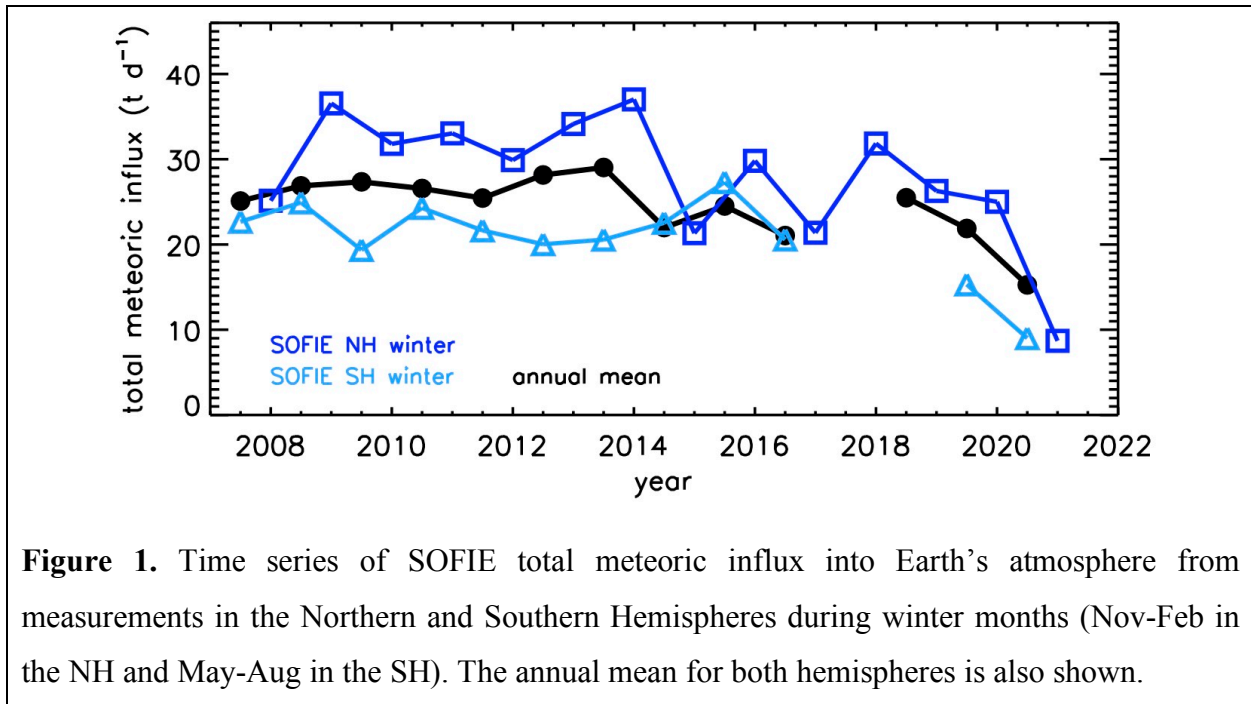
61 observations contain both IPD and ISD, and separating these is important for estimating the
62 meteoric influx at Earth. The Wind ISD results are validated through comparisons with ISD
63 simulations from the Interplanetary Meteoroid environment for EXploration (IMEX) model
64 [Sterken *et al.*, 2015; Strub *et al.*, 2019].

65 **2. SOFIE observations**

66 SOFIE has conducted solar occultation measurements from the Aeronomy of Ice in the
67 Mesosphere (AIM) satellite since 2007 [Russell *et al.*, 2009]. The measurements are used to
68 retrieve vertical profiles of temperature, five gases (O₃, H₂O, CO₂, CH₄, and NO), polar
69 mesospheric cloud (PMC) extinction at 11 wavelengths, and meteoric smoke extinction at three
70 wavelengths (330 - 1037 nm). SOFIE observes primarily polar latitudes, with the exception of
71 2017 - 2019 when orbital progression caused an excursion through the tropics and a change from
72 sunsets in the Southern Hemisphere (SH) to the Northern Hemisphere (NH) (vice versa for
73 sunrises, see *Hervig et al.*, 2021 for details). The current SOFIE data is version 1.3 which is
74 available online (sofie.gats-inc.com).

75 SOFIE smoke measurements have been used to characterize the variation of smoke in
76 height and time, and revealed the chemical composition of smoke [*Hervig et al.*, 2009; 2017]. The
77 smoke extinctions used here are monthly zonal means, avoiding summer measurements when
78 PMCs contaminate the smoke signal [*Hervig et al.*, 2012]. Extinction is converted to volume
79 density for a smoke composition of olivine (Mg_{2x}Fe_{2-2x}SiO₄, $x = 0.4$), which is optically detected
80 by SOFIE. Volume density is then used to derive the ablated meteoric influx through comparisons
81 with smoke simulations from the Whole Atmosphere Community Climate Model (WACCM)
82 [*Bardeen et al.*, 2008; *Hervig et al.*, 2017, 2021]. SOFIE results during 2007-2020 indicate a global
83 mean ablated influx into Earth's atmosphere of 7 ± 2 metric tons per day (t d⁻¹). Since only ~30%

84 of incoming meteoroids are ablated [Carrillo-Sánchez *et al.*, 2020], the corresponding total influx
 85 (ablated plus surviving material) is $25 \pm 7 \text{ t d}^{-1}$. The influx from SOFIE observations are shown in
 86 Figure 1, where the results indicate year-to-year variations and greater influx in the NH than in the
 87 SH. The hemispheric difference is still not understood, but could indicate an asymmetry in
 88 meteoric influx that is not represented in WACCM. The results below consider the meteoric influx
 89 from SOFIE as the average of the NH and SH values.



90 3. Wind observations

91 The Wind spacecraft was launched in 1994 to quantify the dynamics of the Sun-Earth
 92 system [Wilson *et al.*, 2021]. Wind operates within 1° of the ecliptic plane and has orbited the first
 93 Lagrange point (L1) since July 2004 ($\sim 1.5 \times 10^6$ km sunward from Earth). Prior to 2004, Wind
 94 conducted a variety of orbital maneuvers, including petal orbits through the magnetosphere, lunar
 95 flybys, and an excursion to the second Lagrange point [Malaspina and Wilson, 2016; Wilson *et*

96 *al.*, 2021]. Many of these periods are not useful for dust measurements, and were screened from
97 the analyses presented here.

98 Meteoroids are detected when they collide with Wind and a fraction of the spacecraft body
99 is vaporized and ionized [Mann, 2019]. The resulting plasma perturbs the electric potential of
100 spacecraft surfaces [Shen *et al.*, 2021], which is observed by the WAVES electric field antennas
101 and recorded by the Time Domain Sampler (TDS) [Bougeret *et al.*, 1995]. A similar approach has
102 been used for dust measurements by other spacecraft including Voyager [Gurnett *et al.*, 1983] and
103 the Mars Atmosphere and Volatile Evolution Mission (MAVEN) [Andersson *et al.*, 2015]. The
104 Wind dust detector area is the cross-sectional area of the cylindrical spacecraft body (1.8 m height
105 \times 2.4 m diameter), or 4.3 m². Wind is estimated to be sensitive to meteoroids with radii (r) of 0.1
106 - 11 μ m, or 10⁻¹⁴ to 10⁻⁸ g in mass (m) for a dust density of $\rho = 2.65$ g cm⁻³, but cannot resolve the
107 size of individual impactors. Malaspina *et al.* [2014] noted that the lower and upper mass bounds
108 are uncertain by a factor of 10 or more, due to observational uncertainties and assumptions in the
109 measurement interpretation. Wind reports the number of dust detections per day, which represents
110 particles with m from 10⁻¹⁴ to 10⁻⁸ g. The Wind dust observations are discussed in detail by
111 Malaspina *et al.* [2014], Meyer-Vernet *et al.* [2014], Kellogg *et al.* [2016], and Wood *et al.* [2015].
112 Malaspina and Wilson [2016] describe the archived data which are available online
113 (cdaweb.gsfc.nasa.gov). The Wind dust record is summarized in Figure 2, where the monthly
114 average meteoric flux is shown. The results indicate pronounced decadal and annual variations
115 (e.g., more dust in March than September), which are investigated below.

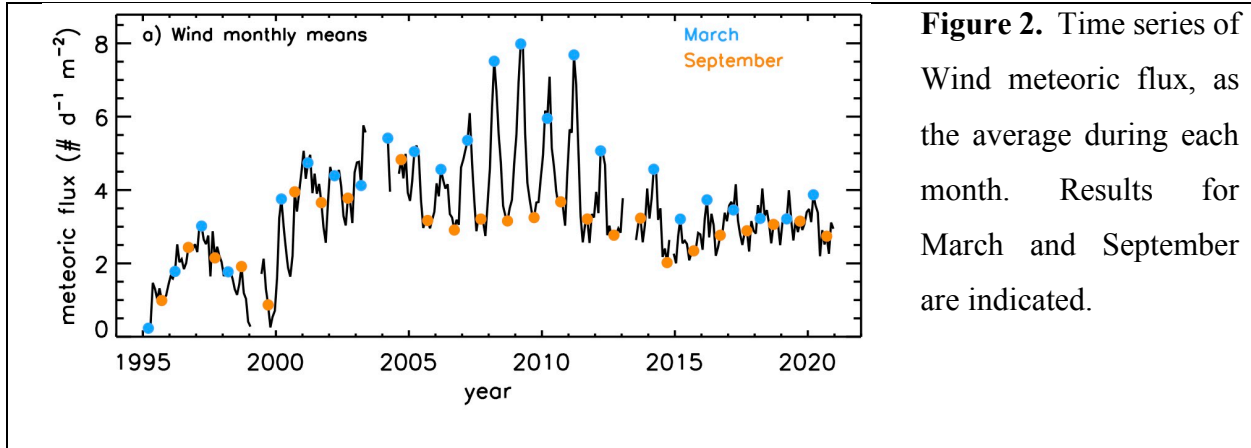
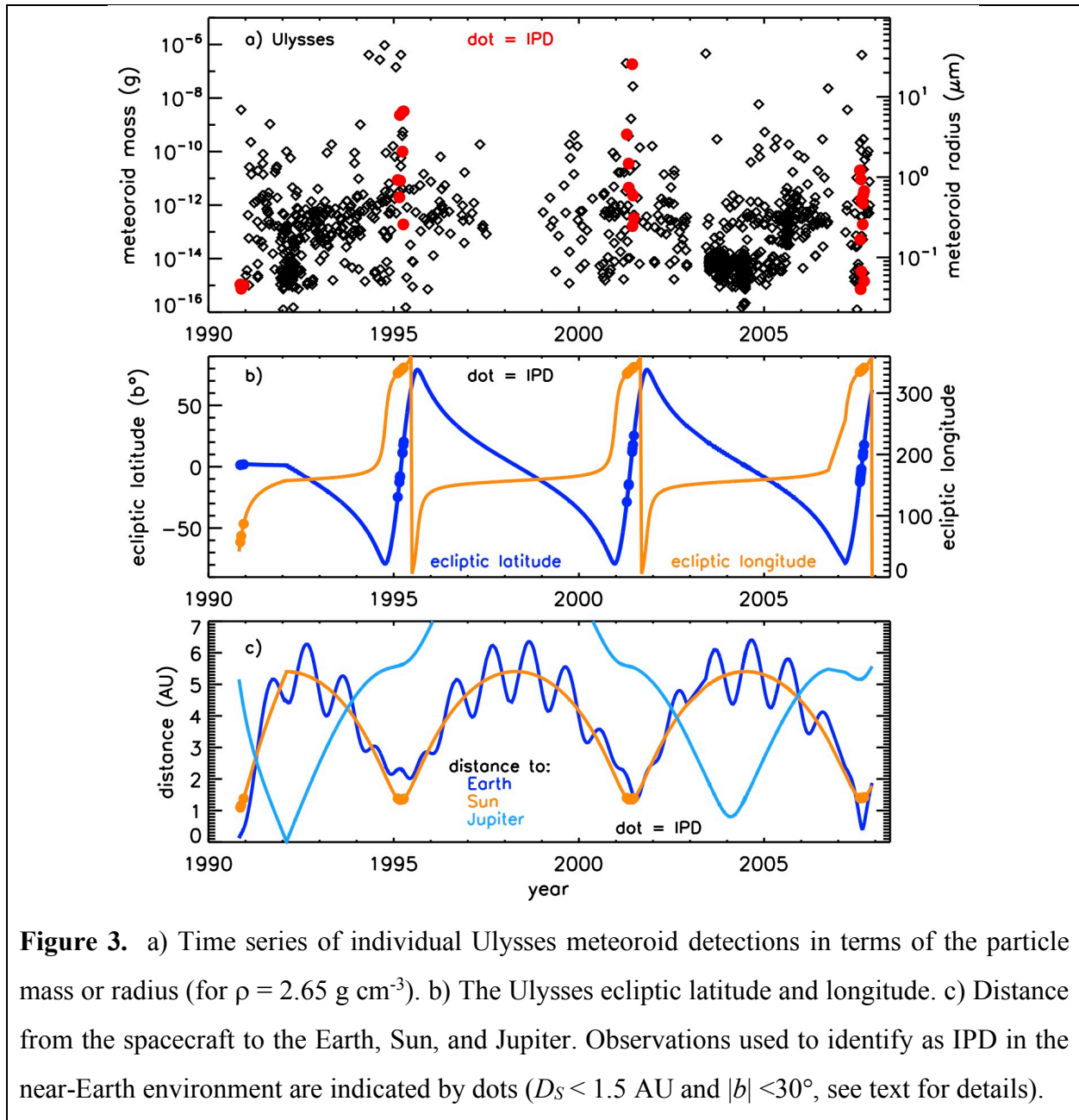


Figure 2. Time series of Wind meteoric flux, as the average during each month. Results for March and September are indicated.

116 **4. Ulysses Observations**

117 Ulysses operated during 1990 - 2007, and was the first spacecraft to conduct a polar orbit
 118 around the Sun. An in situ dust detector used impact ionization to measure the mass of individual
 119 particles with m from $\sim 10^{-16}$ - 10^{-6} g [Grün *et al.*, 1992; Krüger *et al.*, 2006; 2019]. The detector
 120 sensitive area is quoted as a maximum of 0.02 m^2 by Krüger *et al.* [2015], which is the value used
 121 here. The Ulysses dust observations are illustrated in Figure 3a, where the mass and radius of each
 122 particle are shown. The reported particle mass uncertainties are typically a factor of 5 to 10, due
 123 to measurement errors combined with uncertainties in the interpretation. Due to the high-
 124 inclination polar orbit of the Sun, the Ulysses data set consists mostly of ISD. Strub *et al.* [2015]
 125 describe the criteria for identifying ISD in Ulysses, and the present study considered these (in
 126 reverse) to find IPD in the Ulysses record. Particles detected at high ecliptic latitudes (b , Figure
 127 3b) are most likely interstellar in origin [Krüger *et al.*, 2006], since interplanetary dust is
 128 concentrated near the ecliptic plane [e.g., Soja *et al.*, 2019]. Exceptions can occur, however, as
 129 dust from Halley type comets and Oort cloud comets has been detected far above the ecliptic plane.
 130 IPD in the near-Earth environment was identified by considering 1) spacecraft - sun distances (D_s)
 131 of less than 1.5 AU, and 2) relatively low ecliptic latitudes ($|b| < 30^\circ$). These criteria limit the
 132 Ulysses observations to those near perihelion and also exclude the Jupiter flybys (see Figure 3).

133 Note that filtering by rotation angle will not separate IPD from ISD because the interstellar flow
 134 direction was aligned with the heliocentric prograde motion (i.e., the dominant IPD direction) near
 135 perihelion [Strub *et al.*, 2015]. The selection criteria here yields dust observations at an average
 136 D_S of 1.36 AU. These observations occurred during four periods (see Figure 3) comprising a total
 137 of 0.76 years, which is the observing interval used for the Ulysses IPD flux quantities below.



138 **4. Meteoric mass distributions**

139 Interpreting the various measurements and relating them to each other requires an
 140 understanding of the meteoric mass distribution. The mass of meteoroids spans many orders of
 141 magnitude, with ISD ranging from 10^{-16} - 10^{-10} g ($r \approx 0.1$ - $2 \mu\text{m}$, for $\rho = 2.65 \text{ g cm}^{-3}$) and IPDs
 142 spanning roughly 10^{-15} to 10 g ($r \approx 0.1 \mu\text{m}$ to 1 cm) [e.g., *Krüger et al.*, 2019; *Sterken et al.*, 2015].
 143 Visual meteors are roughly 10^{-2} to 10^3 g ($r \approx 0.1$ - 5 cm) but contribute little to the total meteoric
 144 mass influx at Earth, and larger bodies ($m > 1 \text{ kg}$) appear only on geologic time scales. *Grün et al.*
 145 [1985] (G85) described a meteoric mass distribution based on spacecraft in situ observations, lunar
 146 crater analysis, and photometric measurements of the Zodiacal light. The G85 expression yields
 147 the cumulative dust flux in free space, $n_C(m)$ ($\text{g m}^{-2} \text{ s}^{-1}$), for a given m (g) (i.e., the number of
 148 particles with mass $> m$),

$$149 \quad n_C(m) = (2.2 \times 10^3 m^{0.306} + 15)^{-4.38} + 1.3 \times 10^{-9} (m + 10^{11} m^2 + 10^{27} m^4)^{-0.36} +$$

$$150 \quad 1.3 \times 10^{-16} (m + 106 m^2)^{-0.85} \quad (1)$$

151 The number of particles with a given m , $n(m)$, is found from $n(m_i) = n_C(m_i) - n_C(m_{i+1})$. The number
 152 distribution is easily converted to a mass distribution, $f(m) = m n(m)$ [*Grün et al.*, 1985].

153 The G85 expression and observations from Wind and Ulysses describe the meteoric flux
 154 in free space. Relating this to the flux into Earth's atmosphere requires consideration of Earth's
 155 gravity and surface area. The focusing effect of planetary gravity on meteoric dust was described
 156 by *Drolshagen et al.* [2017] as the enhancement factor

$$157 \quad H_F = v^2 / (v^2 - v_{esc}^2) \quad (2)$$

158 where v is the dust velocity (far from Earth) and v_{esc} is the escape velocity (11.1 km s^{-1} for Earth)
 159 [see also *Jones and Poole*, 2007]. The present study assumed a mean dust velocity of 17 km s^{-1}
 160 [e.g., *Borin et al.*, 2017] giving $H_F = 1.74$, which is the value used below. The statistical uncertainty

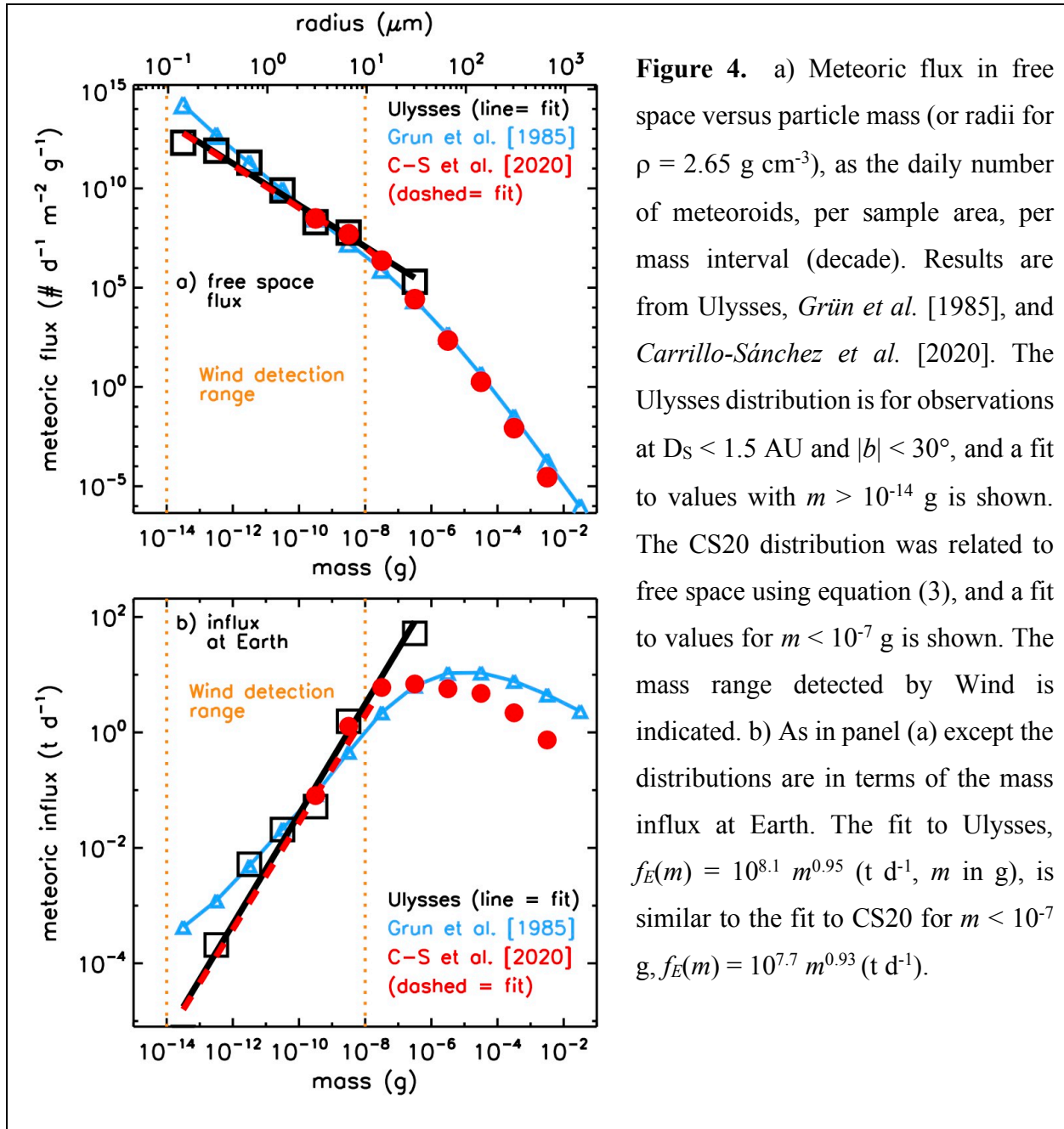
161 in H_F is $\sim 20\%$, for considering v in the range of 14 - 28 km s⁻¹. Earth's surface area is calculated
 162 at the typical meteor ablation altitude of 100 km ($S_E = 5.26 \times 10^{14}$ m²). With these considerations
 163 the total meteoric influx at Earth, F_E , is given by

$$164 \quad F_E = F H_F S_E \quad (3)$$

165 where F is the total flux in free space, $F = \sum f(m)$. Note that this expression is adaptable to the
 166 numeric or mass flux distributions as well (e.g., $f_E(m) = f(m) H_F S_E$, assuming constant v).

167 Ulysses observations in the near-Earth environment (see Section 4) were used to
 168 characterize the IPD mass distribution. The numeric flux distribution from Ulysses is compared to
 169 G85 in Figure 4a, along with results from *Carrillo-Sánchez et al.* [2020] (CS20) which describe
 170 $f(m)$ at Earth based on observations and models. The CS20 distribution (their Figure 1a) was related
 171 to free space here using equation (3). The distributions from Ulysses and CS20 are in good
 172 agreement in the range where they overlap, and a log-linear fit to CS20 for $m < 10^{-7}$ g is very close
 173 to the Ulysses values for smaller particles. The meteoric mass distributions from G85 and Ulysses
 174 were related to Earth using equation (3), and are compared to the CS20 curve in Figure 4b. The
 175 distributions in terms of mass reveal some differences that are not apparent in the number
 176 distributions. In particular, both Ulysses and CS20 indicate lower influx than G85 for the smallest
 177 particles ($m < 10^{-10}$ g), while none of the distributions agree for the largest meteoroids ($m > 10^{-7}$
 178 g). In the case of Ulysses, there are no observations of $m > 10^{-6}$ g, although the meteoric flux in
 179 the interval 10^{-7} to 10^{-6} g is ~ 4 times greater than for CS20 or G85. Note that the meteoric mass
 180 influx at Earth is dominated by particles in the range of 10^{-8} to 10^{-3} g. The sum of the distributions
 181 in Figure 4b gives the total meteoric influx at Earth, with $F_E = 37$ t d⁻¹ for G85 and 28 t d⁻¹ from
 182 CS20. Because Ulysses resolves the meteoroid mass, the individual observations can be added to
 183 give $F_E = 32$ t d⁻¹. This is slightly more accurate than summing the histogram values, which assign

184 the average mass to each interval. The reported Ulysses particle mass uncertainties are typically a
 185 factor of 5 to 10, and this error dominates the uncertainty in F_E . Even with the advantage of
 186 counting statistics (error reduction by N^2) the Ulysses F_E uncertainty is large at 76 t d^{-1} . The above
 187 estimates are in good agreement with SOFIE observations which give $F_E = 25 \pm 7 \text{ t d}^{-1}$ on average
 188 [Hervig et al., 2021].



189

190 The meteoric mass and number distributions (Figure 4) were used to interpret the Wind
191 observations, which do not resolve the mass of an impactor, but rather indicate the total flux of
192 particles within the Wind mass detection range, $N_W = \sum_{m_1}^{m_2} n(m)$, with $m_1 = 10^{-14}$ g and $m_2 = 10^{-8}$
193 g. N_W can be computed from the meteoric size distributions (e.g., Figure 4a), and used to provide
194 and an estimate of the total influx at Earth from Wind,

$$195 \quad F_E = N_W \sum f_E(m) / \sum_{m_1}^{m_2} n(m) = N_W C \quad (4)$$

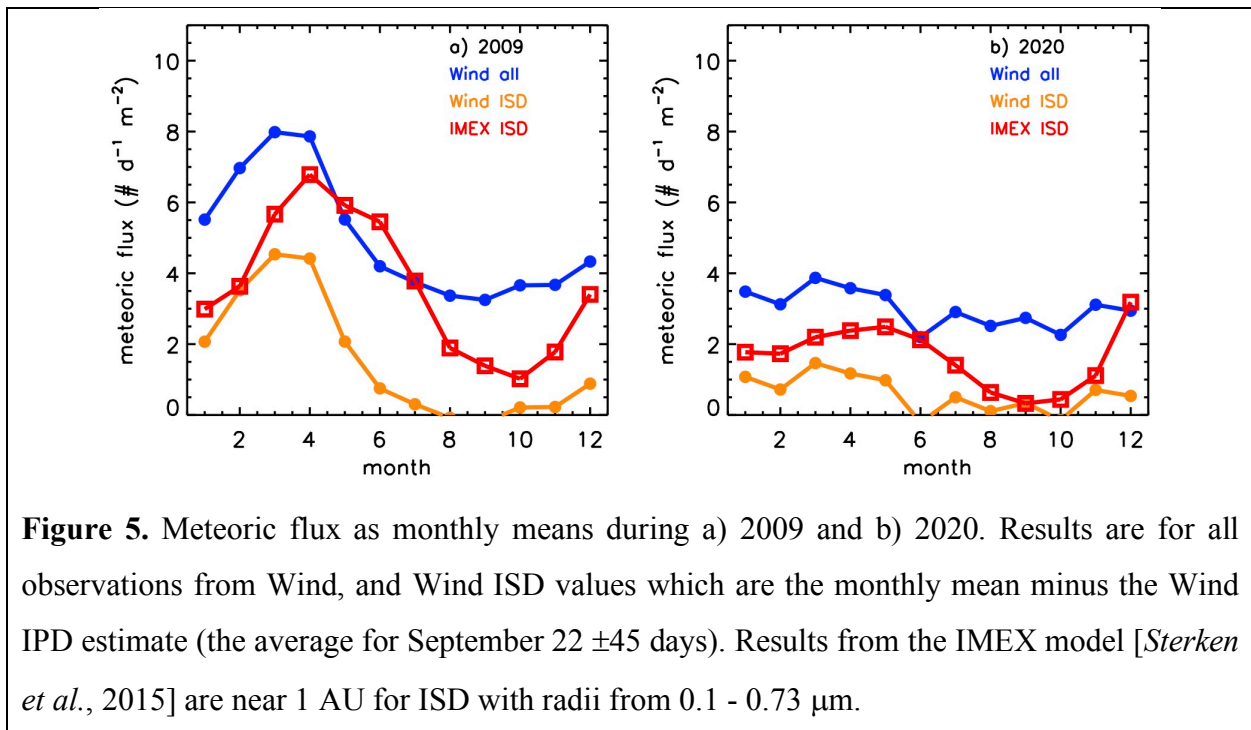
196 In this expression N_W is the Wind observation, and $C = \sum f_E(m) / \sum_{m_1}^{m_2} n(m)$ can be computed from
197 a given modeled or measured mass distribution. Note that the summation of $f_E(m)$ is for the relevant
198 range of IPD (roughly 10^{-9} to 10^{-2} g). For the mass distributions in Figure 4, $C = 2.1$ (t m²) for G85
199 and $C = 11.3$ (t m²) for CS20. One error component in C arise from the factor of 10 uncertainties
200 in the Wind detection limits (m_1 and m_2) [Malaspina et al., 2014]. This error component was
201 estimated to be ~29%, using the Ulysses mass distributions and perturbing m_1 and m_2 alternately
202 by factors of 10 and 0.1. The total uncertainty in C from the G85 distribution is difficult to estimate,
203 but it is at least 35% due to the combined errors in H_F (20%) and in m_1 and m_2 (29%). The
204 uncertainty in C from CS20 is 70% due to errors in F_E , H_F , and m_1 and m_2 . The value for Ulysses
205 was determined directly by summing the individual observations, giving $C = 9.9$ (t m²). The
206 uncertainty in C from Ulysses is close to a factor of ~3, due to the uncertainty in F_E (discussed
207 above) combined with the other terms. The value of C based on G85 is lower than from Ulysses
208 or CS20 because the G85 curve indicates more dust at the smallest sizes. For comparison, the G85
209 distribution gives $N_W = 21.7$ d⁻¹ m⁻², compared to 4.1 d⁻¹ m⁻² from Ulysses and 2.4 d⁻¹ m⁻² from
210 CS20. While the small particles contribute little to the total mass, they contribute greatly to the

211 total number of meteoroids (Figure 4). Equation (4) is used below with Wind observations to
212 examine the IPD influx at Earth.

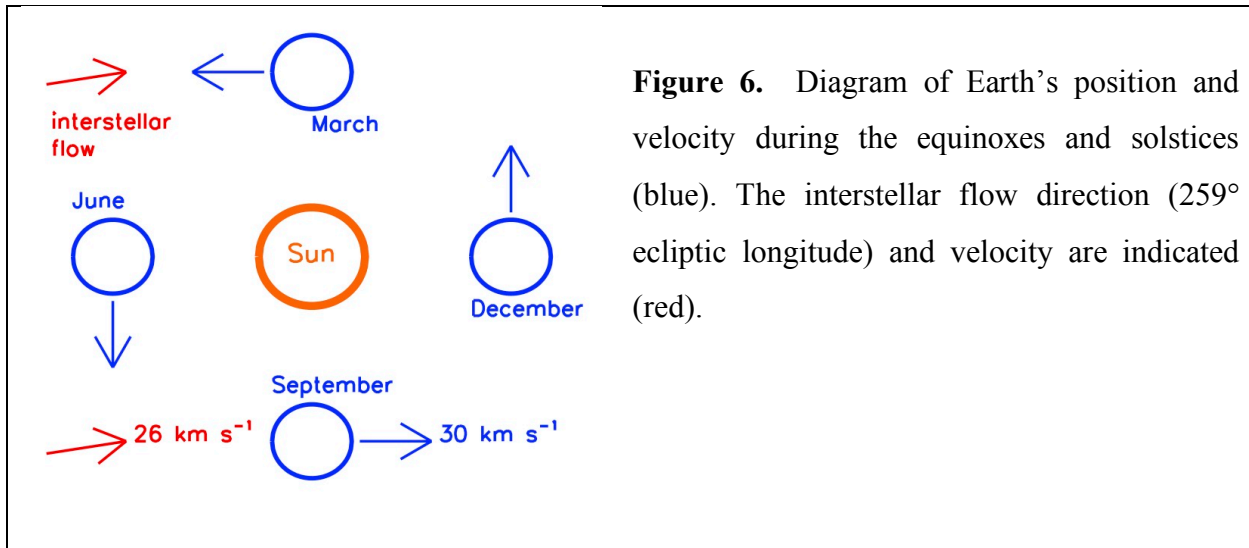
213 **5. Decadal and annual variations in meteoric flux**

214 Wind shows an annual cycle in meteoric flux, that varies in amplitude on a decadal time
215 scale (e.g., Figure 2). The flux annual cycle is examined in greater detail in Figure 5, where the
216 amplitude in 2009 is much larger than in 2020. This annual variation has been discussed by others
217 [Kellog *et al.*, 2016; Malaspina *et al.*, 2014; Wood *et al.*, 2015; Zaslavsky *et al.*, 2012], who
218 concluded that higher flux near the Vernal equinox is associated with ISD. The reason is that
219 Earth's ram direction is into the interstellar flow in March, and away from it in September [see
220 also Malaspina *et al.*, 2014]. Because the Earth's orbital velocity ($\sim 30 \text{ km s}^{-1}$) is similar in
221 magnitude to that of ISD ($\sim 26 \text{ km s}^{-1}$), the ISD flux detected by Wind approaches zero during
222 September, when the velocities are nearly parallel (Figure 6). Given this pattern, Wind
223 observations near the autumn equinox should represent mostly IPD, and an estimate of the IPD
224 flux was determined from Wind as the mean of observations surrounding the autumn equinox
225 (September 22 ± 45 days). It should be noted that the assumption of a constant ISD velocity here
226 is a simplification [e.g., Sterken *et al.*, 2012], and that faster and slower ISD can exist. It is thus
227 possible that Wind measurements in September contain a few ISD, although a more detailed
228 treatment of ISD velocities is beyond the scope of this paper. The ISD flux from Wind was
229 subsequently obtained by subtracting the IPD flux from the monthly mean values during the rest
230 of the year (Figure 5). The approach taken here for isolating IPD and ISD in Wind observations is
231 similar to that used by Wood *et al.* [2015]. The Wind ISD flux shows a strong annual variation,
232 that is consistent with ISD flux simulations from the IMEX model [Sterken *et al.*, 2015; Krüger *et*
233 *al.*, 2019]. The IMEX results shown here are for the near Earth environment (1 AU), and ISD with

234 radii from 0.1 - 0.73 μm . Note that both Wind and IMEX indicate a stronger spring ISD peak in
 235 2009 than in 2020, which is explored below. The model peak occurs slightly later (April) than in
 236 Wind (March), which could be related to the assumed interstellar flow direction (259° ecliptic
 237 longitude) in IMEX. The model peak in ISD would occur at an earlier time if the interstellar flow
 238 was from a higher longitude (roughly 1 day per degree). Indeed, a slightly higher ecliptic longitude
 239 (274°) for ISD was considered by *Sterken et al.* [2014] in an interpretation of Stardust in situ ISD
 240 measurements. In additions, the analysis of Wind and Ulysses observations by *Wood et al.* [2015]
 241 also suggests that the interstellar flow comes from ecliptic longitudes greater than 259° .



242



243

244 Monthly mean ISD flux during 1995 - 2021 from Wind compare favorably to IMEX
 245 simulations (Figure 7a), with both indicating a stronger annual variation and greater overall ISD
 246 flux during 2004 - 2016. The trajectories of ISD in the solar system are controlled by solar gravity,
 247 solar radiation pressure, and magnetic field strength. Theory predicts that ISD flux should correlate
 248 to changes in the solar magnetic field (SMF), due to the Lorentz forces experienced by charged
 249 particles in motion [e.g., *Landgraf et al.*, 2000; *Sterken et al.*, 2015]. The SMF varies with a 22-yr
 250 periodicity (the Hale cycle, see Figure 7c), where the net effect on ISD is a focusing of particles
 251 in the inner heliosphere during solar south pole positive phases. Variations in the ISD flux are
 252 indeed coincident with changes in SMF, and linear regression to annual means gives correlation
 253 coefficients (p) of 0.74 for Wind and 0.67 for IMEX (Figure 7b). The heliospheric current sheet
 254 (HCS) tilt was also examined, which is a representation of the interplanetary magnetic field that
 255 exhibits an 11-yr cycle (in phase with Lyman- α flux). The HCS is considered a factor in ISD
 256 trajectories [*Sterken et al.*, 2015], although the Wind and IMEX ISD are only weakly correlated
 257 with the HCS tilt ($p = 0.1$ for Wind and 0.34 for IMEX). The good agreement between Wind and
 258 IMEX confirms that Wind observations are dominated by ISD during spring. This agreement

259 furthermore suggests that using Wind measurements near the autumn equinox provides a good
 260 approximation of IPD, which is important for characterizing the influx at Earth. Note that the Wind
 261 and IMEX results indicate an ISD influx at Earth (using equation (3)) of less than 0.01 t d^{-1} , which
 262 is insignificant compared to the IPD influx of $\sim 25 \text{ t d}^{-1}$.

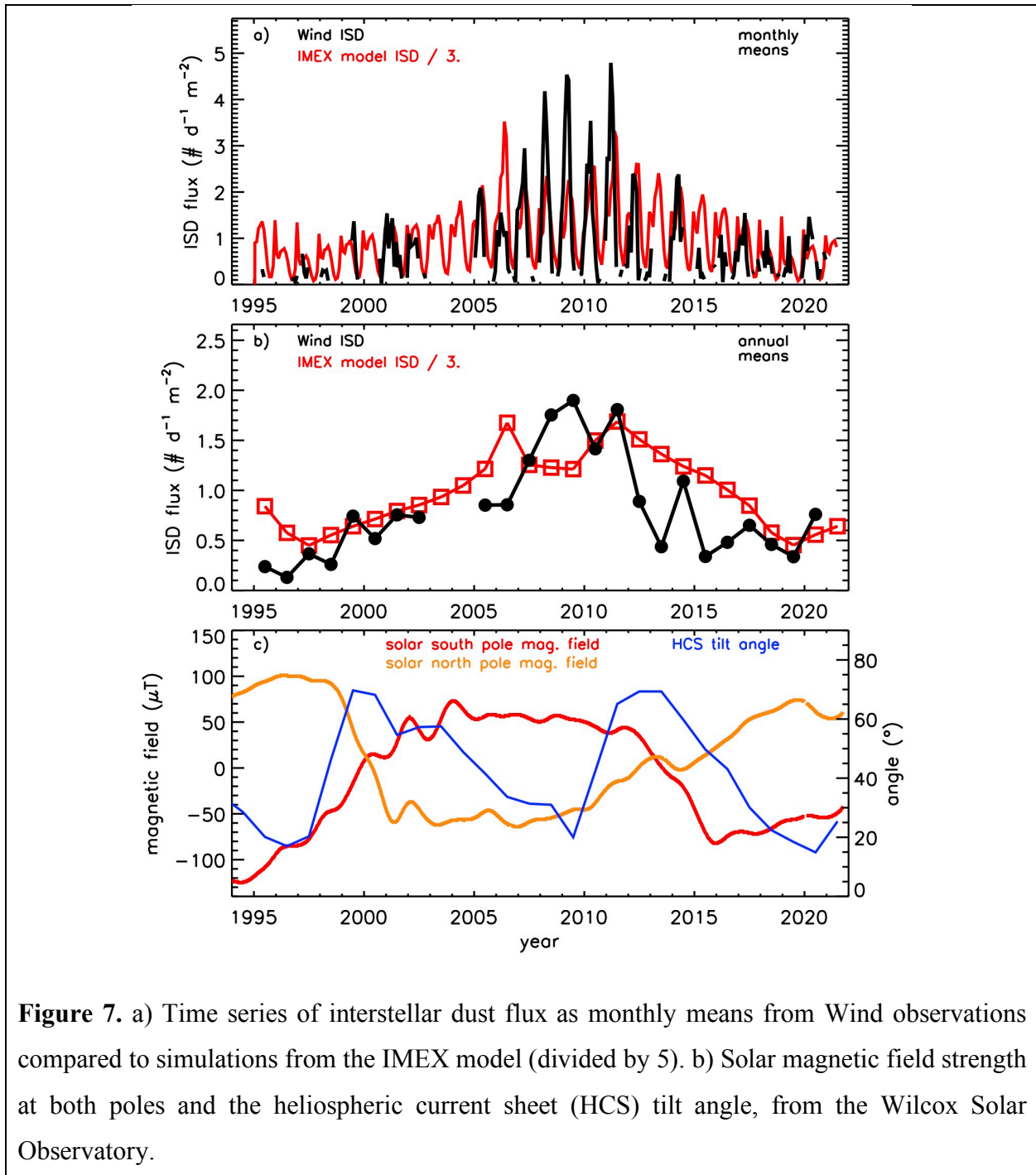


Figure 7. a) Time series of interstellar dust flux as monthly means from Wind observations compared to simulations from the IMEX model (divided by 5). b) Solar magnetic field strength at both poles and the heliospheric current sheet (HCS) tilt angle, from the Wilcox Solar Observatory.

263 Meteoric influx at Earth was estimated from the Wind IPD flux determined as above. The
264 Wind F_E estimates use a constant (equation (4)) that is based on integrating the mass distributions
265 from either Ulysses, G85, or CS20 (see Section 4). Wind F_E determined from the yearly IPD flux
266 values are compared to SOFIE, Ulysses, and CS20 in Figure 8a. Wind F_E using C determined from
267 G85 are much lower than when C from Ulysses or CS20, with the later providing Wind influx
268 estimates that are in reasonable agreement with SOFIE, Ulysses, and CS20. Note that both Wind
269 and SOFIE show similar year-to-year influx variations. The influx time series are compared to the
270 solar magnetic field and HCS tilt angle in Figure 8b. Linear regression indicates a strong F_E - SMF
271 correlation for both Wind ($p = 0.70$) and SOFIE ($p = 0.62$). The correlation with HCS tilt angle is
272 weaker, however, with $p = 0.01$ for Wind and 0.42 for SOFIE. The Wind and SOFIE F_E time series
273 are shown in Figure 8c with a fit to the results based on linear regression to the SMF. These results
274 suggest that changes in the SMF can alter the flow of IPD in the inner heliosphere. This result is
275 not anticipated, however, because IPD have small charge-to-mass ratios (Q/m), unlike ISD. While
276 the IPD response to changing SMF would not be instantaneous, it is possible that a cumulative
277 effect is realized after many orbits of the sun. This idea is supported somewhat by the apparent
278 time delay in changing F_E with respect to SMF. Indeed, the highest F_E - SMF correlation is found
279 for a time lag of 14 months, with $p = 0.76$ for Wind and 0.70 for SOFIE. The agreement between
280 SOFIE and Wind concerning year-to-year and decadal changes in meteoric influx is encouraging,
281 and furthermore suggests that variability in IPD appears in Earth's mesosphere.

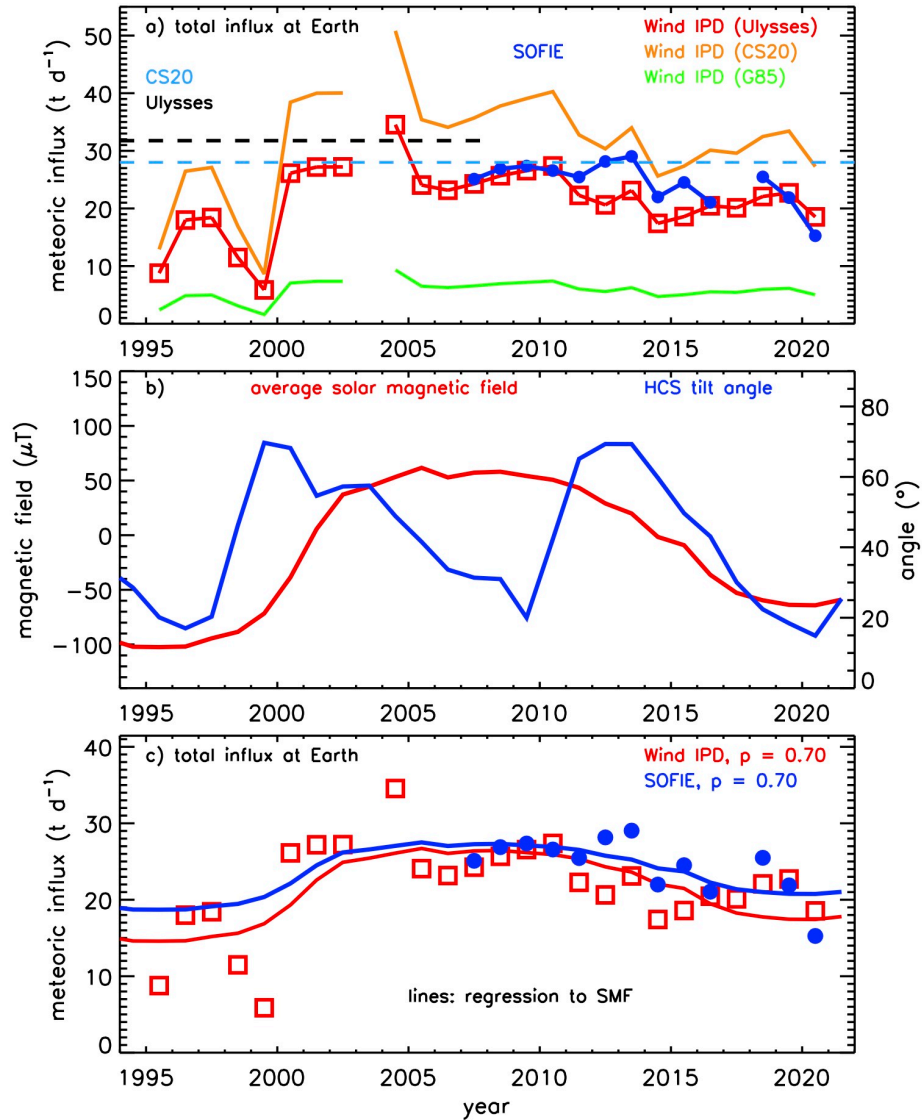


Figure 8. a) Time series of total meteoric influx (F_E) at Earth. Wind results are shown for conversion factors based on the dust distribution from either Ulysses, *Carrillo-Sánchez et al.* [2020] (CS20), or *Grün et al.* [1995] (G85). SOFIE results are the average for winter months near $67^\circ N$ (Nov-Feb) and $67^\circ S$ (Jun-Sep) [*Hervig et al.*, 2021]. The average influx based on Ulysses IPD observations during 1990 - 2007 is indicated ($|b| < 30^\circ$ and $D_s < 1.5$ AU). The CS20 F_E based on observations of iron and sodium in the mesosphere and cosmic spherules collected at South Pole is shown. b) The North-South average solar polar magnetic field strength and HCS tilt angle, as annual means. c) SOFIE and Wind F_E (C from Ulysses), with regressions to the average SMF time series and regression coefficients as listed.

282 The median F_E from Wind during 2007 - 2020 for C determined from the Ulysses, CS20,
 283 and G85 results are 22, 33, and 6 t d⁻¹, respectively, each with a standard deviation of ~14% during
 284 the time period. The median F_E based on the three Wind time series during 2007 - 2020 (i.e., Figure
 285 8a) is 22 t d⁻¹, with a standard deviation of 11 t d⁻¹ (50%) which is due mostly to the spread in C .
 286 The total uncertainty in Wind F_E includes contributions from the error in H_F and uncertainties in
 287 the IPD flux measurements, and is closer to 13 t d⁻¹ (60%). Table 1 summarizes the meteoric influx
 288 estimates from this work and some recent publications.

Table 1. Total meteoric influx (ablated + surviving material) at Earth from different sources.

Source	Method	Meteoric influx (t d ⁻¹)
Wind	Satellite in situ dust detection (2007-2020), <i>this work</i>	22 ± 13
Ulysses	Satellite in situ dust detection (1990-2007), <i>this work</i>	32 ± 76
SOFIE	Satellite remote measurements of meteoric smoke in the mesosphere (2007-2021) [<i>Hervig et al., 2021</i>]	25 ± 7
<i>Carrillo-Sánchez et al. [2020]</i>	Model scaled to measurements of Fe & Na in the mesosphere and cosmic spherules from the South Pole	28 ± 16
<i>Borin et al. [2017]</i>	Long Duration Exposure Facility (LDEF) satellite in situ dust measurements (1984-1990)	15 ± 3
<i>Gardner et al. [2014]</i>	Lidar measurements of Na in the mesosphere	60 ± 16

289 5. Summary

290 This work examined meteoric influx using in situ dust detection by the Wind and Ulysses
 291 spacecraft, and observations of meteoric smoke in the mesosphere by the SOFIE satellite
 292 instrument. Wind does not resolve the mass of the detected meteoroids, but rather reports the total
 293 number of particles with mass from 10⁻¹⁴ - 10⁻⁸ g. The Wind measurements were separated into
 294 the interstellar and interplanetary components. The Wind ISD estimates are in good agreement
 295 with simulations from the IMEX model, in terms of the both the annual and decadal flux variations.
 296 The decadal ISD variation is correlated to the 22-year solar magnetic cycle, as anticipated by
 297 theory and predicted by IMEX. The Wind IPD observations were related to the total meteoric

298 influx at Earth using IPD mass distributions from Ulysses and previous publications. The resulting
299 Wind influx estimates are in good agreement with SOFIE and Ulysses. The SOFIE and Ulysses
300 influx time series show similar year-to-year and decadal changes in meteoric influx. The decadal
301 influx variation exhibits an unanticipated correlation to the 22-year solar magnetic cycle. This
302 relationship may be an artifact, or could indicate that changes in the solar magnetic field can alter
303 the trajectories of interplanetary dust.

304 **Acknowledgements.** This work was funded in part by the AIM mission through NASA contract
305 NAS5-03132. V. J. Sterken received funding from the European Union's Horizon 2020 research
306 and innovation program under grant agreement N 851544. L. B. Wilson was partially supported
307 by Wind MO&DA funds. SOFIE data are available online (sofie.gats-inc.com). WIND meteoric
308 dust data are available online (cdaweb.gsfc.nasa.gov). Wilcox Solar Observatory data are available
309 online (<http://wso.stanford.edu/#MeanField>). Ulysses dust observations are available online
310 (cdaweb.gsfc.nasa.gov).

311 **References**

- 312 Andersson, L., et al. (2015), Dust observations at orbital altitudes surrounding Mars, *Science*, 350,
313 398, doi:10.1126/science.aad0398.
- 314 Bardeen, C. G., O. B. Toon, E. J. Jensen, D. R. Marsh, and V. L. Harvey (2008), Numerical
315 simulations of the three-dimensional distribution of meteoric dust in the mesosphere and upper
316 stratosphere, *J. Geophys. Res.*, 113, D17202, doi:10.1029/2007JD009515.
- 317 Borin, P., G. Cremonese, F. Marzari, and A. Lucchetti (2017), Asteroidal and cometary dust flux
318 in the inner solar system, *A&A*, 605, A94, doi: 10.1051/0004-6361/201730617.
- 319 Bougeret, J., et al. (1995), Waves: The radio and plasma wave investigation on the wind spacecraft,
320 *Space Sci. Rev.*, 71, 231–263, doi:10.1007/BF00751331.

321 Carrillo-Sánchez, J. D.; Gómez-Martín, J. C.; Bones, D. L.; Nesvorný, D.; Pokorný, P. Benna, M.;
322 Flynn, G. F.; Plane, J. M. C. (2020) Cosmic dust fluxes in the atmospheres of Earth, Mars,
323 and Venus, *Icarus*, 335, art. no. 113395.

324 Drolshagen, G., D. Koschny, S. Drolshagen, J. Kretschmer, B. Poppe (2017), Mass accumulation
325 of earth from interplanetary dust, meteoroids, asteroids and comets, *Planetary and Space*
326 *Science*, 143, 21-27, ISSN 0032-0633, <https://doi.org/10.1016/j.pss.2016.12.010>.

327 Gardner, C. S., Alan Z. Liu, D. R. Marsh, Wuhu Feng and J. M. C. Plane (2014), Inferring the
328 Global Cosmic Dust Influx to the Earth's Atmosphere from Lidar Observations of the Vertical
329 Flux of Mesospheric Na, *J. Geophys. Res. Space Physics*, DOI: 10.1002/2014JA020383.

330 Gurnett, D. A., E. Grun, D. Gallagher, W. S. Kurth, and F. L. Scarf (1983), Micron-sized particles
331 detected near Saturn by the Voyager plasma wave instrument, *Icarus*, 53, 236–254,
332 doi:10.1016/0019-1035(83)90145-8.

333 Grün E., Zook H. A., Fechtig H., Giese R. H. (1985), Collisional Balance of the Meteoritic
334 Complex, *Icarus*, 62, 244–272.

335 Grün, E., Fechtig, H., Kissel, J., Linkert, D., Maas, D., McDonnell, J. A. M., Morfill, G. E.,
336 Schwehm, G., Zook, H. A., Giese, R. H (1992) The Ulysses dust experiment, *Astronomy and*
337 *Astrophysics Suppl. Ser*, 92, 411-423.

338 Hervig, M. E., L. L. Gordley, L. E. Deaver, D. E. Siskind, M. H. Stevens, J. M. Russell III, S. M.
339 Bailey, L. Megner, and C. G. Bardeen (2009), First satellite observations of meteoric smoke
340 in the middle atmosphere, *Geophys. Res. Letters*, doi:10.1029/2009GL039737.

341 Hervig, M. E., L. E. Deaver, C. G. Bardeen, J. M. Russell, S. M. Bailey, and L. L. Gordley (2012),
342 The content and composition of meteoric smoke in mesospheric ice particles from SOFIE
343 observations, *J. Atmos. Solar-Terr. Phys.*, doi:10.1016/j.jastp.2012.04.005.

344 Hervig, M. E., Brooke, J. S. A., Feng, W., Bardeen, C. G., Plane, J. M. C. (2017), Constraints on
345 meteoric smoke composition and meteoric influx using SOFIE observations with models, *J.*
346 *Geophys. Res. Atmospheres*, 122, doi:10.1002/2017JD027657.

347 Hervig, M. E., Plane, J. M. C., Siskind, D. E., Feng, W., Bardeen, C. G., & Bailey, S. M. (2021).
348 New global meteoric smoke observations from SOFIE: Insight regarding chemical
349 composition, meteoric influx, and hemispheric asymmetry. *Journal of Geophysical Research:*
350 *Atmospheres*, 126, e2021JD035007. <https://doi.org/10.1029/2021JD035007>.

351 Jones, J., and M. G. Poole (2007), Gravitational focusing and shielding of meteoroid streams, *Mon.*
352 *Not. R. Astron. Soc.* 375, 925–930, doi:10.1111/j.1365-2966.2006.11349.

353 Kellogg, P. J., K. Goetz, and S. J. Monson (2016), Dust impact signals on the wind spacecraft, *J.*
354 *Geophys. Res. Space Physics*, 121, 966–991, doi:10.1002/2015JA021124.

355 Krüger, H., N. Altobelli, B. Anweiler, S.F. Dermott, V. Dikarev, A.L. Graps, E. Grün, B.A.
356 Gustafson, D.P. Hamilton, M.S. Hanner, M. Horányi, J. Kissel, M. Landgraf, B.A. Lindblad,
357 D. Linkert, G. Linkert, I. Mann, J.A.M. McDonnell, G.E. Morfill, C. Polanskey, G. Schwehm,
358 R. Srama, H.A. Zook (2006), Five years of Ulysses dust data: 2000–2004, *Planetary and*
359 *Space Science*, 54, 9–10, 2006, Pages 932-956, ISSN 0032-0633,
360 <https://doi.org/10.1016/j.pss.2006.04.015>.

361 Krüger, H., P. Strub, E. Grün, and V. J. Sterken (2015), Sixteen years of Ulysses interstellar dust
362 measurements in the solar system. I. Mass distribution and gas-to-dust mass ratio, *Astrophys.*
363 *J.* 812, doi:10.1088/0004-637X/812/2/139.

364 Krüger, H., P. Strub, N. Altobelli, V. J. Sterken, R. Srama, E. Grün (2019), Interstellar dust in the
365 solar system: model versus in situ spacecraft data, *Astronomy & Astrophysics*, 626, A37,
366 <https://doi.org/10.1051/0004-6361/201834316>.

367 Landgraf, M., Baggaley, W. J., Grün, E., Krüger, H., & Linkert, G. (2000), Aspects of the mass
368 distribution of interstellar dust grains in the solar system from in situ measurements, *J.*
369 *Geophys. Res.*, *105*, 10343.

370 Malaspina, D. M., M. Horanyi, A. Zaslavsky, K. Goetz, L. B. Wilson III, and K. Kersten (2014),
371 Interplanetary and interstellar dust observed by the Wind/WAVES electric field instrument,
372 *Geophys. Res. Lett.*, *41*, 266–272, doi:10.1002/2013GL058786.

373 Malaspina, D. M. and L. B. Wilson III (2016), A database of interplanetary and interstellar dust
374 detected by the Wind spacecraft, *J. Geophys. Res. Space Physics*, *121*, 9369–9377,
375 doi:10.1002/2016JA023209.

376 Mann, I., L. Nouzák, J. Vaverka, T. Antonsen, Å. Fredriksen, K. Issautier (2019), Dust
377 observations with antenna measurements and its prospects for observations with Parker Solar
378 Probe and Solar Orbiter, *Ann. Geophys.*, doi: 10.5194/angeo-2019-94.

379 Megner, L, D. E. Siskind, M. Rapp, and J. Gumbel (2008), Global and temporal distribution of
380 meteoric smoke; a 2D simulation study, *J. Geophys. Res.*, *113*, D03202,
381 doi:10.1029/2007JD009054.

382 Meyer-Vernet, N., M. Moncuquet, K. Issautier, and A. Lecacheux (2014), The importance of
383 monopole antennas for dust observations: Why Wind/WAVES does not detect nanodust,
384 *Geophys. Res. Lett.*, *41*, 2716–2720, doi:10.1002/2014GL059988.

385 Plane, J. M. C. (2012), Cosmic dust in the earth’s atmosphere, *Chem. Soc. Rev.*, *41*, 6507-6518,
386 doi: 10.1039/c2cs35132c.

387 Rudraswami, N. G., , M. Ppandey, M. J. Genge, and D. Fernandes (2021), Extraterrestrial dust as
388 a source of bioavailable iron contributing to the ocean for driving primary productivity,
389 *Meteoritics & Planetary Science*, *56*, Nr 12, 2175–2190, doi: 10.1111/maps.13764.

390 Russell, J. M. III, et al. (2009), Aeronomy of Ice in the Mesosphere (AIM): Overview and early
391 science results, *J. Atmos. Sol.-Terr. Phys.*, *71*, 289-299, doi:10.1016/j.jastp.2008.08.011.

392 Shen, M. M., Z. Sternovsky, A. Garzelli, D. M. Malaspina (2021), Electrostatic Model for Antenna
393 Signal Generation From Dust Impacts, *J. Geophys. Res.: Space Physics*, *126*, 9, e29645,
394 <https://doi.org/10.1029/2021JA029645>.

395 Soja, R. H., E. Grün, P. Strub, M. Sommer, M. Millinger, J. Vaubailon, W. Alius, G. Camodeca,
396 F. Hein, J. Laska, M. Gastineau⁴, A. Fienga, G. J. Schwarzkopf, J. Herzog, K. Gutsche, N.
397 Skuppin, and R. Srama (2019), IMEM2: a meteoroid environment model for the inner solar
398 system, *Astronomy & Astrophysics*, *628*, A109 (2019), [https://doi.org/10.1051/0004-](https://doi.org/10.1051/0004-6361/201834892)
399 [6361/201834892](https://doi.org/10.1051/0004-6361/201834892).

400 Sterken, V. J., N. Altobelli, S. Kempf, G. Schwehm, R. Srama, and E. Grün (2012), The flow of
401 interstellar dust into the solar system, *A&A* *538*, A102, doi: 10.1051/0004-6361/201117119.

402 Sterken, V.J., Westphal, A. et al., (2014), Stardust Interstellar Preliminary Examination X:
403 Interstellar dust simulations for the Stardust mission. *Meteo. and Planet. Sci.*, *49*, pp. 1690-
404 1697, <https://doi.org/10.1111/maps.12219>.

405 Sterken, V. J., Strub, P., Krüger, H., von Steiger, R. & Frisch, P. (2015), Sixteen Years of Ulysses
406 Interstellar Dust Measurements in the Solar System. III. Simulations and Data Unveil New
407 Insights into Local Interstellar Dust. *Astrophys. J.* *812*, 141, DOI: 10.1088/0004-
408 [637X/812/2/141](https://doi.org/10.1088/0004-637X/812/2/141).

409 Sterken, V. J., Westphal, A. J., Altobelli, N., Malaspina, D. & Postberg, F. (2019), Interstellar Dust
410 in the Solar System. *Space Sci. Rev.* *215*, 43, DOI: 10.1007/s11214-019-0607-9.

411 Strub, P., V. J. Sterken, R. Soja, H. Krüger, E. Grün, and R. Srama (2019), Heliospheric
412 modulation of the ISD flow onto Earth, *A&A*, *621*, A54, <https://doi.org/10.1051/0004->

413 6361/201832644.

414 Wilson, L. B., Brosius, A. L., Gopalswamy, N., Nieves-Chinchilla, T., Szabo, A., Hurley, K., et
415 al. (2021). A quarter century of wind spacecraft discoveries. *Reviews of Geophysics*, 59,
416 e2020RG000714. <https://doi.org/10.1029/2020RG000714>.

417 Wood, S. R., D. M. Malaspina, L. Andersson and M. Horanyi (2015), Hypervelocity Dust Impacts
418 on the Wind Spacecraft: Correlations between Ulysses and Wind Inter- stellar Dust
419 Detections, *J. Geophys. Res. Space Physics*, 120, 7121–7129, doi:10.1002/2015JA021463.

420 Zaslavsky, A., et al. (2012), Interplanetary dust detection by radio antennas: Mass calibration and
421 fluxes measured by STEREO/WAVES, *J. Geophys. Res.*, 117, A05102,
422 doi:10.1029/2011JA017480.

423